npj | flexible electronics

Article

Published in partnership with Nanjing Tech University

https://doi.org/10.1038/s41528-024-00363-7

Unobstructive and safe-to-wear watt-level wireless charger

Sangjun Kim[1,8], Jonathan Wells[2,8], Sarnab Bhattacharya[2], Hamsi Nathan[3], Jiaming He[4], Isabella Tubilla[3], Heeyong Huh[5], Pooja Kakani[2], Ali Farshkaran[2], Praveenkum Pasupathy[2], Jianshi Zhou[4], Emily Porter[2], Nathan Lazarus[6,7] ✉ & Nanshu Lu[1,2,3,4,5] ✉

A wearable microgrid that centralizes and distributes harvested energy across different body regions can optimize power utilization and reduce overall battery weight. This setup underscores the importance of developing cable-free wireless power transfer (WPT) systems for mobile and portable devices to eliminate the risks posed by wired connections, especially in dynamic and hazardous environments. We introduce a thin, stretchable, and safe hand band capable of watt-level wireless charging through the widely adopted Qi protocol operating at 130 kHz. The implementation of non-adhesive fabric encapsulation serves to protect the 50-μm-thin spiral copper antenna from mechanical strain, ensuring an overall hand band stretchability of 50%. We also create a stretchable "Ferrofabric", characterized by a magnetic permeability of 11.3 and a tensile modulus of 75.3 kPa, that provides magnetic shielding for the antenna without compromising wearability. The "Ferrofabric" improves the coil inductance but induces core loss in AC application. By fully understanding and managing loss mechanisms such as the skin effect, proximity effect, core loss, and joule heating, we achieve a wireless charging efficiency of 71% and power delivery of 3.81 W in the kHz frequency range. Our WPT hand band is unobstructive to hand motion and can charge a handheld smartphone as fast as a desktop charger or power a battery-free chest-laminated e-tattoo sensor, with well-managed thermal and electromagnetic safety. Through a holistic electromagnetic, structural, and thermal design, our device culminates in a safe, rugged, and versatile solution for wearable WPT systems.

The growing capabilities of mobile and wearable electronics have amplified the necessity for competent on-body power management, embracing energy harvesting, storage, and utilization[1–4]. To cater to this need, the concept of a wearable microgrid was recently proposed to centralize the storage of power harvested from various parts of the body and to facilitate its distribution among the different devices located at various body regions[5,6]. This microgrid operates through conductive cables or fabrics embedded in clothing, circumventing the body[7–11]. Despite the elaborate setup, it holds several advantages over individually powered devices. These include dynamic power allocation, decreased overall battery weight, and improved user mobility, which are of particular importance for military personnel, first responders, and those involved in the mining industry[12–14]. However, a different challenge arises when it comes to linking external mobile devices such as cell phones or GPS to the centralized carry-on power source through a cable. The power cords of mobile devices pose significant safety hazards of electric shock and entanglements, especially for soldiers in combat and field workers using multiple mobile devices in high-activity and harsh environments[15], emphasizing the need for a safe, cable-free power transfer mechanism supported by wireless power transfer (WPT) specifically targeting the body's extremities, such as the hands and head[16–19].

So far, the researches of on-body WPT have primarily focused on powering wearable and implantable devices operating at milliwatt (mW) power levels[8,20–23]. Contemporary mobile and wearable devices, including cell phones, GPS, smartwatches, and augmented reality (AR) glasses, however, demand power beyond mW levels. Although advancements in wearable energy harvesters like photovoltaic and biomechanical devices demonstrate

[1]Department of Mechanical Engineering, The University of Texas at Austin, Austin, TX, USA. [2]Department of Electrical and Computer Engineering, The University of Texas at Austin, Austin, TX, USA. [3]Department of Biomedical Engineering, The University of Texas at Austin, Austin, TX, USA. [4]Texas Materials Institute, The University of Texas at Austin, Austin, TX, USA. [5]Department of Aerospace Engineering and Engineering Mechanics, The University of Texas at Austin, Austin, TX, USA. [6]Department of Electrical and Computer Engineering, University of Delaware, Newark, DE, USA. [7]US Army Research Laboratory, Adelphi, MD, USA. [8]These authors contributed equally: Sangjun Kim, Jonathan Wells. ✉e-mail: nlazarus@udel.edu; nanshulu@utexas.edu

the possibility of watt-level power generation[24,25], watt-level wearable WPT remains largely unexplored. Challenges lie in striking a balance between wearability, power level, transfer efficiency, and biosafety. The biosafety of wearable WPT primarily concerns thermal and electromagnetic safety. Current watt-level WPT examples, like inductive gloves, use rigid coils which restrict user hand motion[18], deeming them ill-fitted for practical applications.

The surface of the human body is curvilinear and mechanically deformable up to strains of 63% at joints[26]. An ideal wearable WPT should be lightweight and unobstructive to body motion while maintaining mechanical robustness and charging capability. Table 1 offers a summary of various on-body antenna materials, thicknesses, and stretchability[10,11,27–37]. Copper (Cu), the most popular conductive material for antennas due to its high electrical conductivity (5.8×10^7 S/m), is intrinsically stiff and easy to rupture in the form of a freestanding thin film[38]. Stretchable structures such as wrinkles[39] and serpentine ribbons[34,36,40] can enhance stretchability without compromising the intrinsic electrical conductivity of a material, but the configurational change increases the total resistance and takes space. Liquid metal alloys, such as eutectic gallium and indium (EGaIn), are inherently stretchable but have an order of magnitude lower electrical conductivity (3.4×10^6 S/m) than that of Cu, leading to higher power losses and joule heating when built into an antenna[41]. Textile-based antennas can be promising for wearable applications as they can be integrated seamlessly into clothing. However, antennas made with conductive threads still suffer from low charging performance due to their conductivity being equivalent to or lower than EGaIn[31,42–44]. While increasing the conductor thickness could reduce antenna resistance, it would also make the device heavier, less flexible, and more obstructive for users. Furthermore, the stretchable structures and materials for a wearable antenna are prone to changes in coil shape during stretching[40,45], which can weaken the inductive coupling between the transmitter and receiver[46]. Therefore, low-resistance, shape-preserving, and unobstructive-to-wear antennas are yet to be developed.

In addition to the material and structure of the antenna, the operating frequency of WPT, with common options including the Qi protocol (80–300 kHz), near-field communication (NFC) (13.56 MHz), and radio-frequency (RF) (300 MHz–300 GHz) bands, significantly impacts the charging capabilities[47] (see comparisons in Table 1). NFC and RF are commonly used for WPT for wearable and implantable devices operating at μW and mW power levels with a longer charging distance than the Qi procotol[48]. An NFC transmitter mounted on the human body can deliver up to 2 W of power while complying with electromagnetic safety standards, maintaining a specific absorption rate (SAR) ≤ 1.6 W/kg as regulated by the Federal Communications Commission (FCC) guidelines[49]. However, smartphones can potentially reach SAR levels up to 1.59 W/kg[50], leaving little margin for additional SAR contributions from WPT. Furthermore, NFC or higher frequency ranges are also susceptible to body-loading effects causing losses in efficiency[10,11,21,51]. The Qi protocol supports watt-level wireless charging of most commercially available mobile devices without concerns for human safety[37], but the charging performance of wearable antennas consisting of liquid metal or conductive threads operating in this frequency range is limited due to a low transmitter quality factor[52]. Although a liquid metal coil showed a received power of 1.92 W at 110 kHz with a quality factor of 9.5, the 1-mm-thick antenna and the non-stretchable ferrite sheet for magnetic shielding rendered the device cumbersome to wear[35]. To enable versatile wireless charging of both mobile and wearable devices, it is essential to design a safe-to-wear transmitter antenna compatible with the Qi protocol that provides sufficient charging efficiency and power transfer. However, the underlying loss mechanisms, such as the skin effect, proximity effect, and core loss, as well as their interplay, are yet to be fully elucidated for wearable antennas. Safety risks associated with overheating and electromagnetic energy absorption by the tissue should be carefully assessed to ensure that they are within the safety limits.

Magnetic backplanes made of materials such as ferrite have been widely adopted in WPT systems to increase energy storage density and improve coupling[46]. When applied for on-body WPT, magnetic backplanes can also help reduce body-loading effects and electromagnetic energy absorption by the tissue. However, ferrite is intrinsically stiff and brittle. Stretchable magnetic backplanes such as Ferroelastomers, have been developed to replace the rigid ferrite for applications such as soft robotic actuators, sensors, and bioelectronics[33,46,53–59] (see a summary in Supplementary Table 1). Ferroelastomers were fabricated by mixing magnetic particles, including molypermalloy, carbonyl iron, and Sendust, at a relatively low volume fraction (up to 33%[54]), with a silicone matrix, such as the Ecoflex 00-30 and polydimethylsiloxane (PDMS). Typically, the magnetic particles are assumed to be evenly distributed and have a weak interaction with other particles such that the composite behavior follows effective medium theory[54]. Ferroelastomers have successfully achieved a low Young's modulus of 33.3 kPa and an ultrahigh stretchability of 425%[33]. However, the relative magnetic permeability of the composite reached merely 2.9[54], despite the magnetic fillers with permeability as high as 36,000[46,54]. High magnetic permeability backplanes are essential for WPT as they can enhance inductance and quality factor of an inductor. One promising candidate with sufficient magnetic properties is ferrofluid which consists of hydrocarbon oil and magnetic nanoparticles[60,61]. Since the magnetic particles can almost freely optimize their configuration in the liquid medium under an external magnetic field, the magnetization is higher than all reported Ferroelastomers. However, the application of ferrofluid to wearable WPT systems has never been explored due to their fluidity. Although conductive materials such as metals, MXene, graphene, and carbon nanotube can also serve as electromagnetic interference shielding[62], they reduce coil inductance and quality factor due to the eddy current generated in the shielding layer, rendering them unsuitable for WPT applications[63].

Table 1 offers a summary of the state-of-the-art on-body WPT systems[10,11,27–37]. It focuses on features germane to on-body applications such as antenna thickness, device stretchability, WPT frequency, power, efficiency, and SAR. To comprehensively assess power and efficiency, we present the DC input power (P_{In}), AC transmitted power (P_{Tx}), AC received output power ($P_{Out,Rx}$), and DC output power ($P_{Out,Bat}$) of our system, while also specifying the available values from the literature for comparison. It is evident that the previous on-body WPT systems did not always report SAR and have fallen short in simultaneously achieving stretchability, watt-level power transfer, and high WPT efficiency, rendering them incapable of charging both mobile and wearable devices on the body while upholding human safety standards.

Consequently, a comprehensive investigation simultaneously addressing the material, structural, electromagnetic, and thermal aspects is necessary to push the frontier of wearable WPT systems. In particular, elucidating various loss mechanisms is essential and fundamentally helpful for other antenna designs. In this work, we report a palm-worn WPT system capable of powering both mobile and wearable devices compatible with the prevailing Qi protocol. The system is holistically designed via a coupled electromagnetic-structural-thermal analysis (Fig. 1a). For high-efficiency inductive coupling, we adopted a planar Cu coil as the transmitter antenna. The ultrathin Cu antenna is highly flexible and its in-plane stretch can be isolated through non-adhesive fabric encapsulation. For magnetic shielding, we invented a stretchable, high permeability magnetic fabric named "Ferrofabric", which is made by wetting a bamboo fabric with ferrofluid encapsulated by polyurethane. We conducted systematic parametric studies on the coil material and thickness, Ferrofabric size, charging distance, misalignment, as well as electrothermal effects to balance the losses and ultimately, optimize the charging performance. The stretchable WPT hand band is capable of wirelessly charging a handheld smartphone (Fig. 1b) and a chest-laminated e-tattoo sensor (Fig. 1c). The smartphone charging rate is on par with commercial desktop wireless chargers and the wireless dual-mode cardiac sensing e-tattoo[64] can operate without any battery. Through simulations and experiments, long-term thermal and electromagnetic safety is confirmed.

Results and discussion

Multiphysics considerations for a wearable WPT hand band

Figure 1a illustrates the multiphysics considerations for the design of the WPT hand band, which was constructed using a 0.5-mm-thin 20%

Table 1 | State-of-the-art on-body WPT systems

	On body	Antenna material	Antenna thickness	Charging distance	Stretchability (%)	Protocol	Frequency	Tx power	Output power	WPT efficiency (%)	SAR (W/kg)	On-body charging target
This work	Tx	Cu	50 μm	1 mm	50	Qi	130 kHz	7.94 W	3.41 W	42.94 (P_{In} to $P_{Out,Bat}$)	0.002 (local)	Smartphone, e-tattoo
								5.35 W	3.41 W	64.93 (P_{Tx} to $P_{Out,Bat}$)		
								5.35 W	3.81 W	72.33 (P_{Tx} to $P_{Out,Rx}$)		
[35]	Tx	GaInSn	1 mm	2 mm	–	–	110 kHz	3.2 W	1.92 W	60 (P_{Tx} to $P_{Out,Bat}$)	–	Headset, LED, fan, smartphone
[37]	Tx	–	80 μm	2 mm	–	Qi	142 kHz	1 W	230 mW	23 (P_{In} to $P_{Out,Bat}$)	–	Wearable sensors
[28]	Tx	–	–	30 mm	–	–	240 kHz	1.8 W	18 mW	1 (P_{Tx} to $P_{Out,Bat}$)	0.172 (10 g)	Neural stimulator implant
[30]	Tx	PZT/Metglas	120 μm	0	–	–	250 kHz	2.22 mW	9.66 μW	0.435 (P_{In} to $P_{Out,Bat}$)	0.3	Implantable sensors
[27]	Tx	Cu	400 μm	40 mm	–	–	1.3 MHz	4.5 W	297 mW	6.61 (P_{In} to $P_{Out,Bat}$)	–	Gastric stimulator implant
[33]	Tx	EGaIn	1 mm	–	100	–	3 MHz	–	–	–	–	LED
[11]	Tx	Cu	25 μm	20 mm	–	NFC	13.56 MHz	–	–	–	–	Wearable sensors
[31]	Tx	GaInSn	635 μm	10 mm	–	NFC	13.56 MHz	100 mW	4.8 mW	48 (P_{Tx} to $P_{Out,Bat}$)	–	Wearable sensors
[29]	Tx	Cu	80 μm	30 mm	–	ISM	433 MHz	230 mW	1.15 mW	0.5 (P_{In} to $P_{Out,Bat}$)	–	Implantable sensors
[10]	Tx	Cu/Ni	200 μm	–	–	ISM	2.4 GHz	100 mW	10.5 mW	10.5 (P_{Tx} to $P_{Out,Rx}$)	–	Wearable sensors
[34]	Rx	Cu	18 μm	–	20	NFC	13.56 MHz	200 mW	–	–	–	E-tattoos
[32]	Rx	AgNFs	3 μm	0	100	RF	20 MHz	100 μW	40 μW	40 (P_{Tx} to $P_{Out,Rx}$)	–	Signal and voice detection
[36]	Rx	Cu	7 μm	1 mm	25	–	44.5 MHz	187 mW	32.2 mW	17.2 (P_{Tx} to $P_{Out,Rx}$)	–	Wearable sensors

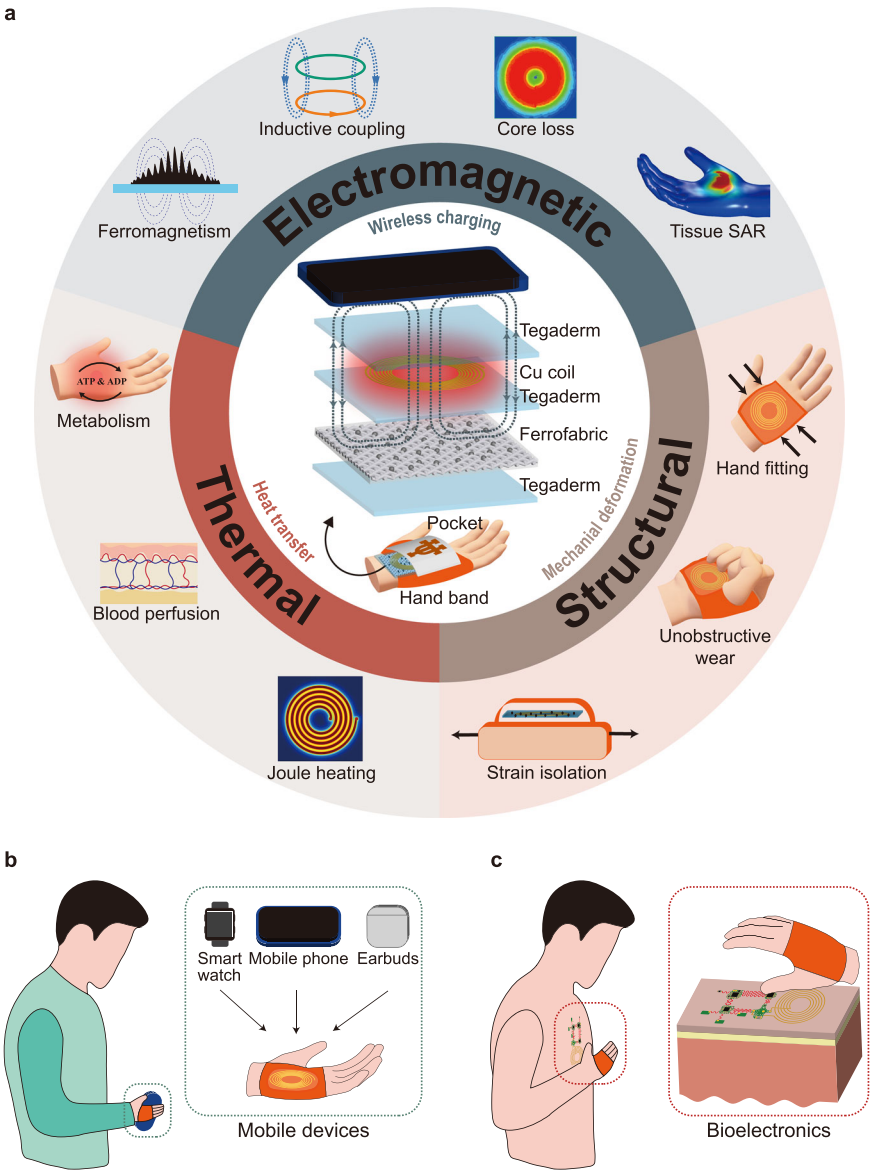

Fig. 1 | The holistic design and multiphysics analysis of an unobstructive hand band as a safe and versatile wearable WPT system. a Schematic illustration of the construction of the hand band and the electromagnetic-structural-thermal analysis that has been performed for it. Conceptual illustrations of wearable wireless charging in two daily use scenarios: **b** mobile devices and **c** wearable electronics.

spandex/80% nylon fabric such that it could fit comfortably to the human palm without compromising any hand movement or functionality. A square-shaped pocket, on the hand band houses a flexible planar Cu coil and a stretchable magnetic backplane, as shown at the bottom of the central schematic. The 50-μm-thin Cu coil, serving as a Tx antenna, can inductively couple with an Rx antenna built-in to mobile or wearable devices when the two are in close proximity. The Ferrofabric was positioned beneath the coil to provide magnetic shielding. The three-layer 3M Tegaderm tape made from polyurethane serves as both encapsulation layers for the Ferrofabric and electrical insulation for the Cu coil.

During on-body WPT, a variety of physical phenomena are involved due to the alternating current (AC) flowing through the Cu coil, which are illustrated in the ring of Fig. 1a. Within electromagnetic considerations, the inductive coupling between the Tx and the Rx is influenced by the ferromagnetism of the Ferrofabric. The AC flow leads to variations in current density within the conductor, such as the skin effect and the proximity effect, causing energy losses. Additionally, core loss induced by magnetic backplanes contributes to an increase in effective antenna resistance and a reduction in charging efficiency. Besides, tissue SAR should be quantified to ensure the electromagnetic safety. Within structural considerations, the hand band needs to fit not too tight or too loose to the hand and should not obstruct any hand movement or functionality. To ensure stable charging even under mechanical deformation, the coil strain is purposely isolated from the stretching of the hand band through the pocket insertion. Within thermal considerations, the flow of current through the coil is accompanied by joule heating that can potentially cause skin burns. Blood perfusion and metabolism also affect skin temperature. The subsequent sections provide detailed descriptions of each physical phenomenon and elaborate on the methodologies implemented to address them.

Ferrofabric as a stretchable magnetic backplane

Wireless charging through inductive coupling can benefit from the use of magnetic backplanes placed under the coils to direct the magnetic flux surrounding the coils and therefore improve the inductance of the coils and ultimately, the coupling coefficient[46]. Supplementary Table 1 summarizes state-of-the-art stretchable magnetic materials that have been developed for stretchable/flexible devices such as WPT systems, actuators, microelectromechanical systems (MEMS), and sensors[33,46,53–59,61]. It is evident that while Ferroelastomers have become significantly more stretchable, they continue to suffer from low magnetic permeability.

We, therefore, introduce a new type of stretchable magnetic backplane combining stretchable fabric with ferrofluid, named Ferrofabric, to

achieve higher magnetic permeability. A commercial ferrofluid (EMG 900, Ferrotec) consisting of surfactant-coated magnetite nanoparticles (~10 nm) dispersed in hydrocarbon oil was used as the magnetic filler. The surfactant and carrier fluid prevent nanoparticles from agglomerating or settling[61] to enhance magnetic shorting, which leads to a low-reluctance pathway for magnetic circuit and consequently, higher permeability (~19.6)[65] (Supplementary Fig. 1). Figure 2a illustrates the fabrication process of the Ferrofabric, wherein an oleophilic fabric (Bamboo Rayon 4 Way Stretch with Spandex, APC Fabric Store) with a thickness of 0.5 mm was selected as the ferrofluid absorber. This bamboo fabric was chosen for its high ferrofluid absorption capacity and mechanical compliance (Supplementary Fig. 2). It can also maintain its shape under both wet and dry conditions. To prevent leakage of the ferrofluid from the Ferrofabric, stretchable transparent polyurethane dressings (Tegaderm, 3M) with a thickness of 47 μm were used for encapsulation. The optical micrographs of the unencapsulated bamboo fabric and Ferrofabric did not exhibit any mechanical failure under 50% uniaxial tensile strain (Fig. 2b). In addition to stretching, the encapsulated Ferrofabric is also easy to bend and twist (Fig. 2c). The mechanical properties of the different layers are offered in Fig. 2d. The bare fabric and the Ferrofabric were tested to have a comparably low modulus (57.5 and 75.3 kPa, respectively, Fig. 2d inset). In addition, both Tegaderm encapsulated bare fabric and Ferrofabric exhibited almost identical moduli (3.60 and 3.51 MPa, respectively), indicating that the presence of ferrofluid had minimal impact on the mechanical behaviors of the encapsulated bamboo fabric.

To investigate the ferromagnetism of the Ferrofabric, magnetization M was measured using a Superconducting Quantum Interference Device (SQUID) by sweeping magnetic field H from −1 T to 1 T at room temperature (Fig. 2e). The H-field induces configurational changes of ferromagnetic nanoparticles in the carrier fluid, aligning them with the field and resulting in higher magnetization (Fig. 2e lower inset). The magnetization of the bare fabric (black) is negligible compared to that of ferrofluid (green) and Ferrofabric (red). The low hysteresis observed in the M–H curves of the ferrofluid and the Ferrofabric indicates low loss and therefore, suitability for AC applications[66]. The relative magnetic permeability of the ferrofluid and the Ferrofabric ($\mu_r = \chi + 1$, where χ is the magnetic susceptibility, i.e., the slope of the M–H curves) is extracted to be 16.6 and 11.3, respectively (Fig. 2e upper inset). The use of the bamboo fabric as the matrix allows the ferrofluid to form continuous magnetic paths, offering more substantial magnetic shorting and hence much higher magnetic permeability (11.3) compared to that of the Ferroelastomers (2.9)[54]. Figure 2f is an Ashby plot that compares the mechanical compliance, i.e., the inverse of Young's modulus, and the relative magnetic permeability of various stretchable ferromagnetic composites and magnetite, the magnetic filler used in ferrofluid. Notably, our Ferrofabric stands out as a mechanically soft but effective ferromagnetic material, making it particularly suitable for wearable WPT devices. Specifically, higher magnetic permeability helps improve charging performance as it directly affects coil inductance and quality factor. Finite element analysis (FEA) indicates that the Ferrofabric can enhance coil inductance by 21.7% due to better shielding effects whereas Ferroelastomers only made an improvement up to 6.1% (Supplementary Fig. 3).

However, oil molecules can potentially permeate through the Tegaderm encapsulation due to large free volume and high polymer chain mobility of polyurethane[67]. To examine the effect of ferrofluid drying, long-term magnetic properties of the Ferrofabric was tested by measuring the impedance of a Cu coil placed on the Ferrofabric (Fig. 2g) because the complex magnetic permeability $\mu = \mu' - j\mu''$ affects both the inductance and effective resistance of a nearby inductor with AC excitation[68]. Supplementary Fig. 4 and Fig. 2h present the long-term changes of the weight and the mechanical and electrical properties of the Tegaderm-encapsulated Ferrofabric. As shown in Supplementary Fig. 4a, b, even though the total weight of the Ferrofabric gradually decreased till Day 20, the effective Young's modulus of the Tegaderm-encapsulated Ferrofabric remained almost unchanged. This implies that the initial weight loss was mainly due to the drying of the excessive carrier fluid rather than that absorbed by the threads. After 20 days, the effective Young's modulus of the Ferrofabric started increasing, suggesting that the absorbed ferrofluid began drying. Notably, the impedance of the Cu coil on the Ferrofabric did not show significant change over 90 days (Supplementary Fig. 4c, d and Fig. 2h), demonstrating long-term stability of the electromagnetic properties of the Ferrofabric despite the changes in the mechanical properties due to the oil drying. This surprising discovery can be attributed to the uniform deposition of magnetite nanoparticles onto the bamboo fabric fibers, which can form magnetic paths to maximize magnetic shorting even long after the carrier fluid dried (Supplementary Fig. 5).

Design of the WPT hand band

Existing research in stretchable and wearable WPT systems typically utilizes a unique charging scheme that only works for a specific application and is not widely adaptable to devices where one does not have control of both the Tx and the Rx sides of the system[35]. Furthermore, they typically have a low amount of power transmitted or received[69]. To create a versatile system capable of charging commercial mobile devices at a watt level as well as a wearable e-tattoo at a microwatt level, our system employs the Qi protocol.

An operating frequency of $f = 130$ kHz was chosen since it is the default frequency of the commercial Qi chargers we use (WCT-NXQ1TXH5 & WCT-15W1CFFPD, NXP). Each board came with an MP-A11 transmitter coil complying with the Qi specifications. The operating frequency highly impacts the AC resistance of the coil, the system's core losses, quality factors, and charging performance[46]. Therefore, optimizing the charging efficiency at this frequency is particularly important in watt-level power transfer to avoid overburdening portable energy sources, prolonging charging time, or compromising human safety due to higher current levels. This requires a comprehensive understanding of all the loss mechanisms within the wearable WPT.

Our wearable Qi-compatible charger consists of a Cu Tx coil with Ferrofabric as the magnetic backplane, as illustrated by Fig. 3a. The Tx coil is a planar spiral with an outer diameter $d_{\mathrm{Tx}} = 51$ mm (Supplementary Fig. 6), which is designed to be smaller than the size of the user's palm. The built-in coil in a smartphone or on an e-tattoo would serve as the Rx coil. The circuit diagram of the WPT system is offered in Fig. 3b where each coil is represented by an inductor (L) and a resistor (R) connected in series with a negligible parasitic capacitor (C) (phase angle of 85° at 130 kHz). Supplementary Fig. 6c also shows the operating frequency of 130 kHz is far below the coil's self-resonant frequency of 7 MHz, validating the coil's parasitic capacitance has a minimal effect on power transfer[70]. For inductive coupling, the maximum coil-to-coil WPT efficiency $\eta_{\max}$ can be calculated by

$$\eta_{\max} = \frac{k^2 Q_{\mathrm{Tx}} Q_{\mathrm{Rx}} \sqrt{1 + Q_{\mathrm{Rx}}^2 + k^2 Q_{\mathrm{Tx}} Q_{\mathrm{Rx}}}}{k^2 Q_{\mathrm{Tx}} Q_{\mathrm{Rx}} \left(1 + \sqrt{1 + Q_{\mathrm{Rx}}^2 + k^2 Q_{\mathrm{Tx}} Q_{\mathrm{Rx}}}\right) + \left(1 + \sqrt{1 + Q_{\mathrm{Rx}}^2 + k^2 Q_{\mathrm{Tx}} Q_{\mathrm{Rx}}}\right)^2 + Q_{\mathrm{Rx}}^2} \quad (1)$$

where $Q = 2\pi fL/R$ and k stand for the quality factor of each coil and the coupling coefficient between them, respectively (Supplementary Note 1 and Supplementary Fig. 7). Equation (1) clearly indicates that higher quality factors and coupling coefficients are desirable to maximize the WPT efficiency. Since the charging distance was measured to be 1 mm for smartphone charging and 0.5 mm for e-tattoo charging, the coupling coefficient k remained close to the maximum value of 1 (0.85 and 0.80, respectively). Hereafter, we keep the WPT frequency, the coil's planar configuration, and the coupling coefficient unchanged, with a primary focus on optimizing the WPT efficiency through the quality factor, and particularly the coil resistance. In terms of coil materials, Cu and EGaIn are considered, both of which have been widely used as flexible antennas.

At 130 kHz, the effective resistance of a conductor is higher than its DC counterpart due to three different loss mechanisms: the skin effect ($R_{\mathrm{Skin\ effect}} \propto 1/\delta$, with skin depth $\delta = \sqrt{1/(\pi f \sigma \mu)}$), the proximity effect

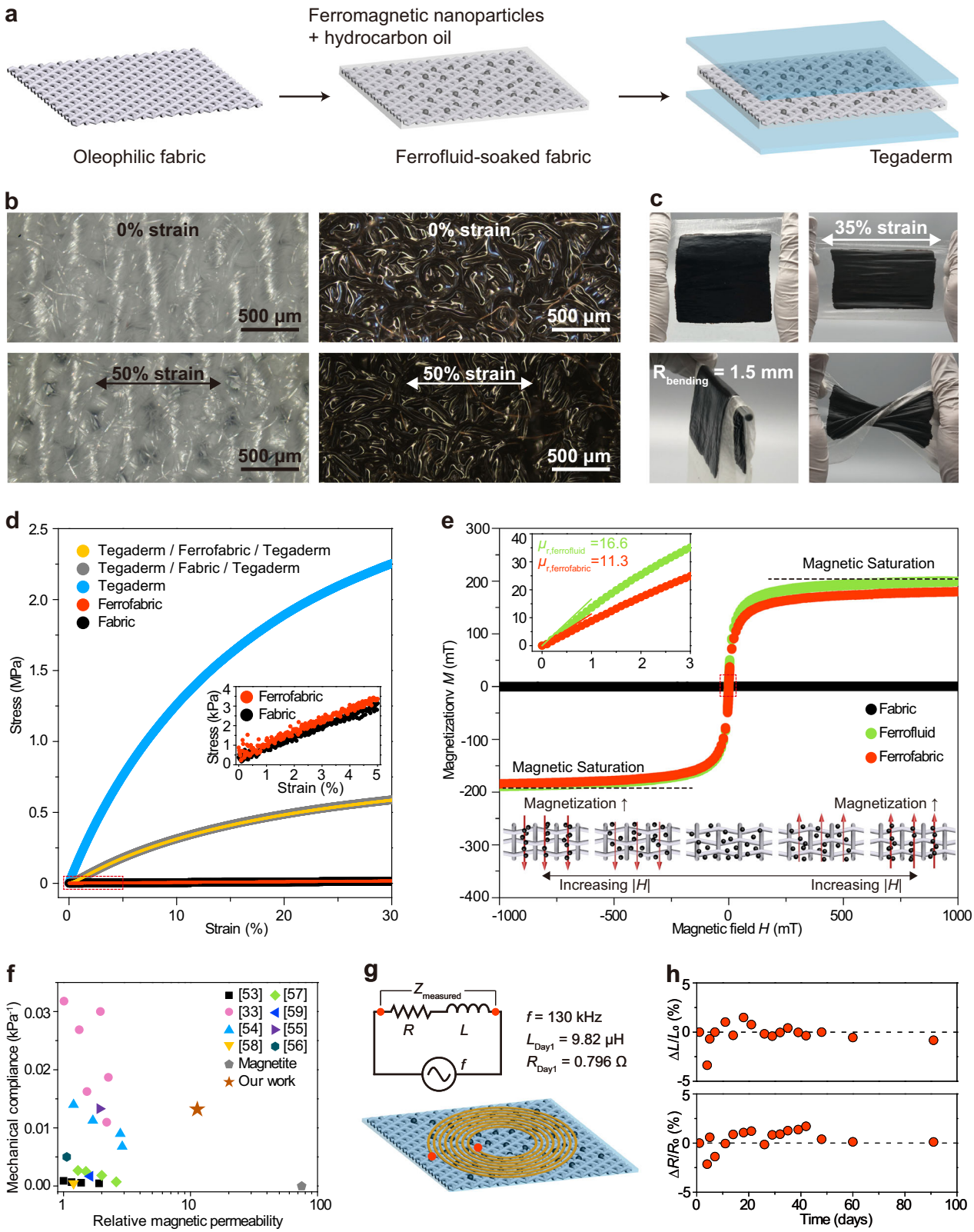

Fig. 2 | Fabrication and characteristics of the Ferrofabric as a stretchable magnetic backplane. a Fabrication process of the Ferrofabric. **b** Optical microscope images of bare bamboo fabric and the Ferrofabric in undeformed and 50% stretched configurations. **c** The Ferrofabric under different deformations: stretching, bending, and twisting. **d** Stress vs. strain curves of bare fabric and Ferrofabric, with and without Tegaderm encapsulation. **e** Magnetization vs. magnetic field curves of the bare fabric, the ferrofluid (EMG 900), and the Ferrofabric. **f** Comparison of mechanical compliance and magnetic permeability with conventional stretchable magnetic composites. **g** Schematic illustration of the long-term measurement of a Cu coil on Ferrofabric. **h** Relative changes in resistance and inductance of a Cu coil on Ferrofabric over 91 days.

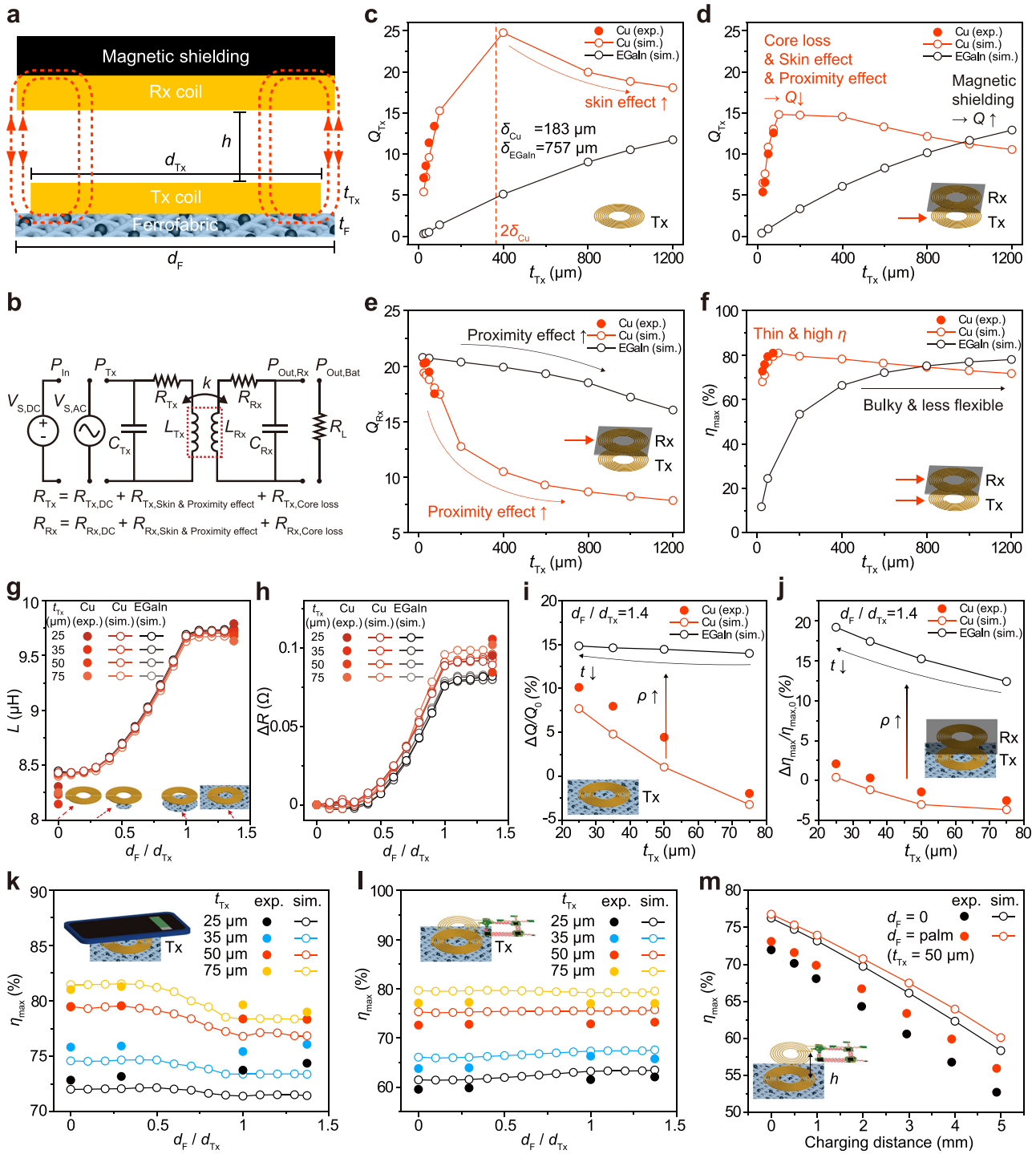

Fig. 3 | Effects of various loss mechanisms on the WPT performance. a A side view of the model of the transmitter (Tx) and receiver (Rx) coil with magnetic backplanes. t_{Tx} denotes the Tx coil thickness. d_F and d_{Tx} are the diameters of the Ferrofabric and the Tx coil, respectively. h is the coil-to-coil distance or the charging distance. **b** Circuit diagram of the WPT system with inductive coupling. **c**–**f** Comparison of antennas made of two commonly used materials: Cu and EGaIn. **c** Quality factor vs. Tx coil thickness considering the skin effect. **d** The effect of various loss mechanisms on the quality factor of the Tx coil inductively coupled to an Rx coil with built-in magnetic shielding of a smartphone. **e** The quality factor of the Rx coil with respect to the Tx coil thickness. **f** Maximum charging efficiency vs. the Tx coil thickness. **g**–**j** Effects of the Ferrofabric placed under the Tx coil on the charging performance of the Cu and EGaIn Tx coils. **g** Tx coil inductance vs. the Ferrofabric size. **h** Changes in Tx coil's AC resistance vs. the Ferrofabric size. **i** Relative changes in the quality factor vs. Tx coil thicknesses when the Ferrofabric is the same size as the fabric pocket, i.e., $d_F/d_{Tx} = 1.4$. **j** Relative changes in maximum charging efficiency vs. Tx coil thicknesses when $d_F/d_{Tx} = 1.4$. **k**–**m** Comparison between modeled (hollow markers) and measured (solid markers) maximum charging efficiencies. **k** Effects of the Ferrofabric size in the smartphone charging case. **l** Effects of the Ferrofabric size in the e-tattoo charging case. **m** Effects of the charging distance in the e-tattoo charging case.

($R_{\text{Proximity effect}} \propto t_{\text{Tx}}, \sigma$), and the core loss ($R_{\text{Core loss}} \propto \mu''$, d_{F}), where σ and d_{F} stand for coil conductivity and Ferrofabric size, respectively. By modeling the skin effect in a straight conductor with a rectangular cross-section using COMSOL FEA (details in "Methods" section), we found that there is an optimal thickness for Cu to exhibit a local minimum of AC resistance (R_{AC}) accounting for the skin effect but not so for EGaIn (Supplementary Fig. 8). In general, thicker coils have lower DC resistance (R_{DC}), as indicated by the black markers in Supplementary Fig. 8a, c. However, under AC, the skin effect becomes nonnegligible when the conductor thickness exceeds 2δ. Given that Cu has a much smaller skin depth than EGaIn (δ_{Cu} =183 μm, δ_{EGaIn} = 757 μm), the skin effect only affects Cu but not EGaIn in the thickness range we considered. Tx coils made of either Cu or EGaIn with multiple thicknesses were simulated to assess the influence of the skin effect on the quality factor (Fig. 3c). A peak in the quality factor of a Cu Tx coil can be clearly identified but it is not the case for EGaIn. We only carried out experiments for Cu coils and those results are plotted as solid markers in Fig. 3c and the rest of Fig. 3.

When an Rx coil is added to the system and all three loss mechanisms are considered (Fig. 3d), the Cu Tx coil quality factor is generally reduced from Fig. 3c whereas the EGaIn Tx coil quality factor is almost unimpacted. While magnetic shielding improves the inductance of the Tx coil, it also elevates the effective resistance by reducing skin depth and introducing core loss. Moreover, the vicinity of the Tx and Rx coils further increases the effective resistance, primarily due to the proximity effect which affects both coils. Therefore, the quality factor of the Rx coil declines not only due to the presence of the Tx coil but further decreases with more conductive and thicker Tx coils (Fig. 3e). Considering the interplay between the loss mechanisms, Fig. 3f indicates that both the Cu and EGaIn antennas can achieve the maximum coil-to-coil WPT efficiency of ~80% with 50 μm < t_{Cu} < 100 μm and t_{EGaIn} > 1200 μm, respectively. However, thicker coils would make the WPT system bulkier and heavier, which clearly hampers wearability. Subsequently, we only consider coil thicknesses that are <100 μm.

To investigate the effects of the size of the Ferrofabric on the charging performance, we placed the Ferrofabric with various sizes under the Tx coil made of either Cu or EGaIn of different thicknesses without the Rx coil (Fig. 3g–i). As evidenced in Supplementary Fig. 4c, d, the Ferrofabric simultaneously increases the inductance and the effective resistance of the antennas. The inductance (Fig. 3g) and the resistance (Fig. 3h) varied when the Ferrofabric size was tuned between the inner and outer diameter of the Tx coil. The inductance of the Tx coil increases with the increase in Ferrofabric size, up to 15% when the Ferrofabric size is 1.4 times the Tx coil size (Fig. 3g). The core loss-induced increase in the effective resistance is independent of the coil materials or thickness (Fig. 3h and Supplementary Fig. 9a, b) because the core loss only depends on the AC frequency and the magnetic flux, which are not affected by the coil material or thickness[71]. As the Ferrofabric reduces the skin depth when μ>1, the Cu coil that is more susceptible to the skin effect exhibits slightly higher increases in the effective resistance than that of the EGaIn coil when all losses are considered (Fig. 3h). Therefore, the Ferrofabric can impact both the quality factor (Fig. 3i and Supplementary Fig. 9c) and charging efficiency (Fig. 3j and Supplementary Fig. 9d). But it only improves the charging efficiency of a system with less conductive Tx coil, such as those made of EGaIn or ultrathin copper. Although the Ferrofabric eventually turned out to be not helpful to the charging performance of our Cu Tx coils due to its counteracting effects of simultaneously improving the inductance and effective resistance, it still plays a role in protecting the underlying tissue from electromagnetic radiation, which is to be discussed in the safety section.

We evaluated the maximum WPT efficiency while charging a commercially available smartphone as well as a custom-built wireless chest e-tattoo sensor[64] connected to a Cu Rx coil identical to the Cu Tx coil in the hand band (Fig. 3k–m). For smartphone charging (Fig. 3k and Supplementary Fig. 10), the maximum coil-to-coil efficiency remained above 70%, even with the thinnest Cu coil used (25 μm). However, the efficiency slightly decreases with a bigger Ferrofabric size due to the additional core loss caused by the built-in magnetic backplane of the smartphone. Figure 3l and Supplementary Fig. 11 show that the maximum efficiency when charging a chest e-tattoo is slightly improved by the Ferrofabric when the Tx coil is thin enough. This is because while the resistance change due to the core loss is independent of the coil thickness, the fraction of the core loss-induced resistance increase is smaller in thinner coils. Subsequently, a 50-μm-thick Cu coil with a Q_{Tx} of 10.9 was adopted in our wearable charger because it has a bending rigidity ($\propto t_{\text{Tx}}^3$) 70% lower than the 75-μm-thick coils whose Q_{Tx} is 12.0 while the efficiency is only compromised by <3%. The effect of charging distance was also investigated since clothing can reside between the chest e-tattoo and the hand band charger (Fig. 3m and Supplementary Fig. 12). The measured efficiency increased from 52.8% (without Ferrofabric) to 56.0% (with Ferrofabric) at the charging distance of 5 mm. The measured efficiencies are slightly lower than the modeled ones due to error propagation from a minor discrepancy in resistance and coupling coefficient values (Supplementary Fig. 12a, d, i). The same results for smartphone charging are offered in Supplementary Fig. 13. It is worth noting that in the case of smartphone charging, there is a crossover in the efficiencies with (red) and without (black) the Ferrofabric at the charging distance of 3 mm (Supplementary Fig. 13j), which indicates that the magnetic shielding effect becomes more prominent than the core loss and the proximity effect combined as the charging distance increases. In addition to the vertical distance between two coils, horizontal misalignment also affects charging performance. Supplementary Fig. 14 shows the simulated charging performance when the two coils have horizontal misalignments in the case of smartphone charging and e-tattoo charging. Since horizontal misalignment reduces the coupling coefficient, charging efficiency drops accordingly. Since the internal Tx coil and the UT logo on the surface of the hand band were designed to align, misalignment can be mitigated by aligning the UT logo on the hand band with the Rx coil.

Electromechanical and electrothermal characteristics of the WPT hand band

To ensure wearability and stable charging, a fabric hand band with a pocket over the palm was designed and fabricated through sewing. A 0.5-mm-thin 20% spandex/80% nylon fabric was chosen over other fabrics due to its high flexibility and stretchability (up to 50%). The fabric band was designed to have a snug fit to the wearer's hand, while the Cu coil and the Ferrofabric were inserted into the fabric pocket which was located at the center of the palm to best align with the Rx coil in a handheld smartphone. Without added adhesives, the free sliding between the coil and the fabric pocket can isolate the stretch of the band from the Cu coil (Fig. 4a). We confirmed that the diameter of the Cu coil remained constant when the band was stretched up to 50% (Fig. 4b), resulting in less than 1% change of the electrical characteristics of the Cu coil (Fig. 4c). The Cu coil and Ferrofabric were subjected to various hand motions such as clenching, hand shaking, and grabbing materials. Although coil deformation and the proximity of conductive and magnetic objects can affect the inductance and resistance of the Cu coil[72], its electrical properties can recover to the original state, ensuring the electromechanical reliability under practical use (Fig. 4d). The Cu coil inside the hand band showed durability under cyclic loadings such as 20% fabric stretching up to 1000 cycles (Fig. 4e) and palm clenching up to 500 cycles (Supplementary Video 1).

One of the key concerns to be addressed in the design of a wearable watt-level WPT system is the hand temperature rise caused by coil joule heating. The long-term thermal safety threshold of human skin is 43 °C[73]. A 3D steady-state heat transfer FEA model was developed using COMSOL for the case of wireless charging of a smartphone (details in "Methods" section), which involves much higher power transfer compared to e-tattoo charging (Fig. 4f). The detailed geometric and material properties are given in Supplementary Fig. 15. This heat transfer model took into account a variety of heat sources including joule heating of both Tx and Rx coils, smartphone operation, tissue metabolism, and the interplay between blood perfusion and tissue temperature[73]. Figure 4g plots the simulated temperature along

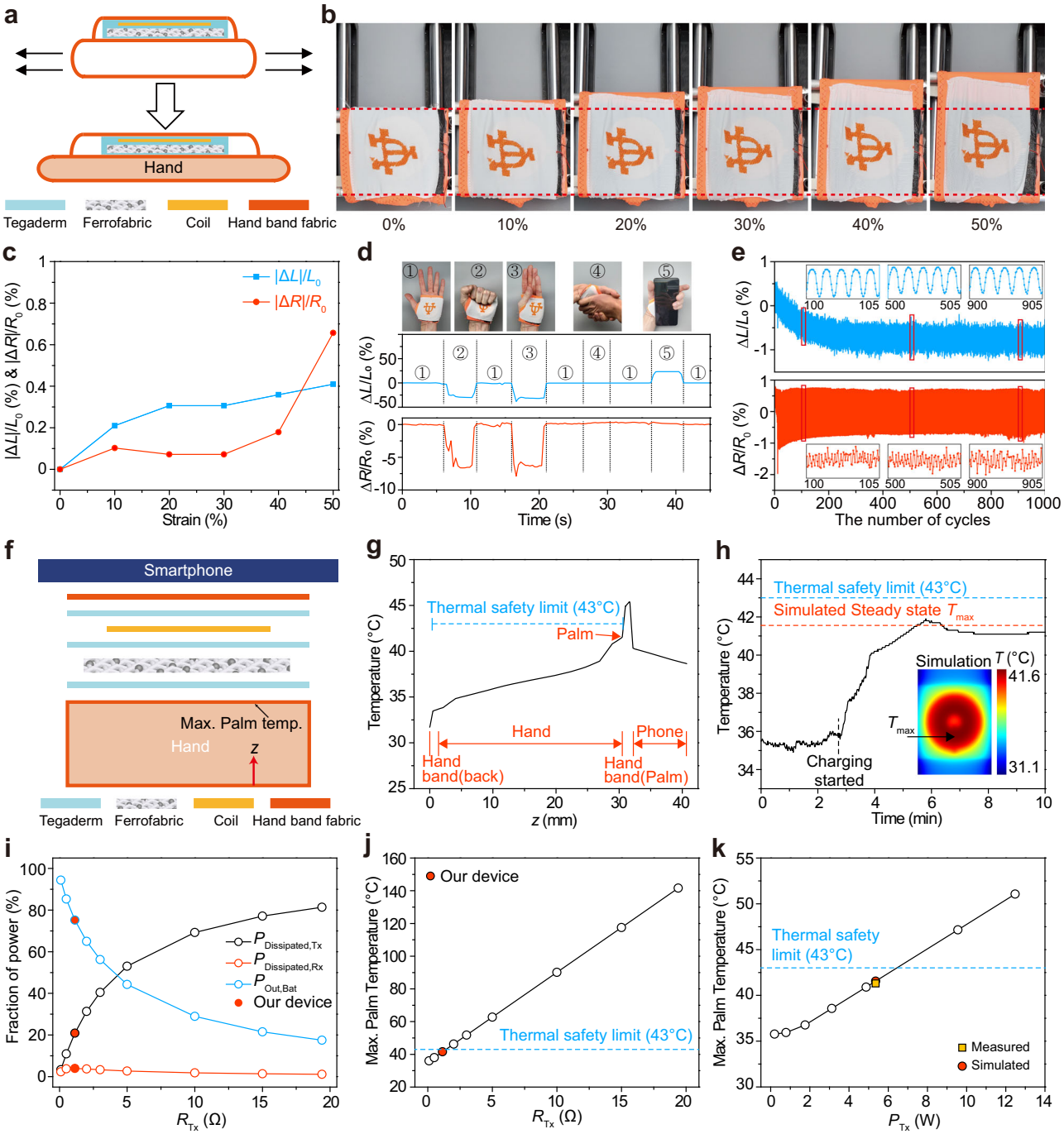

Fig. 4 | Mechanical robustness and thermal safety of our WPT hand band. a Strain isolation by means of a non-adhesive hand band pocket. **b** Demonstration of strain isolation when the hand band was stretched up to 50%. **c** Relative changes in resistance and inductance of the Tx coil during the hand band stretching. **d** Recovery of the relative changes in resistance and inductance after various hand deformations: stretching, clenching, warping, hand shaking, and holding a smartphone. **e** Resistance and inductance of the Cu coil changed <2% after 1000 cycles of 20% stretch of the hand band. **f** Cross-sectional view of the thermal simulation of the in-hand wireless charging of the smartphone to evaluate thermal safety. **g** Simulated temperature in the depth direction of the model shown in (**f**). **h** Measured palm temperature during smartphone charging. The inset shows the temperature distribution of the palm calculated from the steady-state heat transfer simulation. **i** Fractions of power division with respect to Tx resistance. **j** Maximum palm temperature vs. Tx resistance. **k** Effect of transmitted power on maximum palm temperature.

the depth direction originating from a point with peak palm surface temperature as indicated by the inset in Fig. 4h. The simulation result indicates that the entire tissue temperature did not exceed 41.6 °C, which is below the safety threshold of 43 °C. This result is further validated through experimental measurements of palm surface temperatures during smartphone charging on the palm. For real-time temperature monitoring, a thermistor was placed at the peak temperature point as indicated by the simulation (see the inset of Fig. 4h). The measured palm surface temperature gradually increased after charging started and reached a steady-state temperature of 41.3 °C, which is in excellent agreement with the simulated value, confirming the thermal safety of our wearable WPT hand band (Fig. 4h).

Considering that joule heating is a major source of energy dissipation in a WPT system, the resistance of the Tx coil and power level can effectively modulate joule heating and enhance the output power delivered to the

smartphone battery. Figure 4i sheds light on the influence of the Tx coil resistance on the overall power dynamics within the WPT system. This offers insights into the distribution of active power between each coil and the battery, irrespective of power levels (Supplementary Note 1). Note that the AC resistance of the Tx coil is considered in this context. A Tx coil with higher AC resistance leads to reduced output power to the battery, subsequently diminishing WPT efficiency (Supplementary Fig. 16a). Regarding thermal characteristics, a greater portion of heat dissipation is induced by the Tx coil with higher resistance, ultimately leading to the possibility of surpassing the safety threshold (Fig. 4j). Therefore, a Tx coil with high resistance is detrimental to both charging efficiency and thermal safety. Any coil materials with reduced electrical conductivity (e.g., EGaIn or MXene) or coil geometry with increased total length (e.g., serpentine) need to compromise the power transfer levels to comply with the thermal safety threshold. Additionally, EGaIn is susceptible to resistance increase under mechanical deformation, which leads to unreliable charging performance owing to its high deformability[45]. This relationship can also be understood in terms of quality factor, which exhibits an inverse relationship with resistance (Supplementary Fig. 16b). Through the coupled electromagnetic-mechanical-thermal analysis, we have demonstrated the effectiveness of a 50-μm-thick Cu coil as the optimal Tx antenna for a wearable WPT hand band, capable of safely sending out 5.35 W from the palm charger (Fig. 4k).

On-body wireless charging of mobile and wearable devices

To operate our wearable WPT system, suitable commercial Qi charging boards and power specifications were selected and modified to establish a compatible interface with commercial smartphones (Supplementary Note 3). The Qi charging board needed to connect to a battery which served as the power source. After optimizing the WPT hand band design from components to the system, we demonstrated the wireless charging of both a smartphone (Fig. 1b) and a chest e-tattoo (Fig. 1c) as a daily use scenario. The fabric band was worn on the hand to wirelessly charge a smartphone held in the palm (Fig. 5a and Supplementary Video 2). The in-hand charging performance (1% battery capacity increase every 1 min and 49 s) was found to be comparable to that of a commercial desktop wireless charger (Mi Wireless charger MDY-09-EU, Xiaomi) (1% every 2 min and 9 s) (Fig. 5b). Note that all charging rates decreased after reaching a battery capacity of 95% due to trickle charging, meaning lowering the charging voltage to the battery to avoid damaging the battery.

To evaluate the WPT and efficiency of our device in real use, voltage and current waveforms were measured to calculate the active power ($P = V_{\mathrm{rms}} I_{\mathrm{rms}} \cos\varphi$) (Supplementary Fig. 17 and "Methods" section). To provide a comprehensive evaluation, our power measurements were conducted at four key locations: DC input power (P_{In}), AC transmitted power (P_{Tx}), AC received output power ($P_{\mathrm{Out,Rx}}$), and DC output power ($P_{\mathrm{Out,Bat}}$), as labeled in Fig. 3b and Supplementary Fig. 7a. Here, we primarily focus on P_{Tx} to $P_{\mathrm{Out,Rx}}$ efficiency, i.e. the coil-to-coil efficiency as it is what we try to optimize in this work. Figure 5c and Supplementary Fig. 18 illustrate the measured power levels at these four locations during wireless charging of the smartphone with our hand band. Within the normal charging range (0–95% of battery capacity), the P_{In}, P_{Tx}, $P_{\mathrm{Out,Rx}}$, and $P_{\mathrm{Out,Bat}}$ were measured to be 7.94, 5.35, 3.81, and 3.41 W, respectively. The ratio of $P_{\mathrm{Out,Rx}}$ to P_{Tx} renders a coil-to-coil charging efficiency of 71%. The P_{In}, P_{Tx}, $P_{\mathrm{Out,Rx}}$, and $P_{\mathrm{Out,Bat}}$ using the commercial Qi charger were measured to be 7.02, 5.64, 4.42, and 2.86 W, corresponding to a coil-to-coil efficiency of 78% (Supplementary Fig. 17b, c), which is only slightly higher than our hand band charger.

In addition to mobile devices, wearable electronics, like e-tattoos[4,22], can also benefit from WPT integrated into fabrics, eliminating or reducing the need for batteries[7–11,74]. For the charging of these e-tattoos, we demonstrated two modes of operation: battery-free and a depleted battery. Note that our WPT system can be inserted into fabric pockets attached to areas of clothing that are directly over the e-tattoos, extending beyond just the hand band demonstrated in our example. The battery-free case showed that the operation of the e-tattoo, the physiological signals obtained by the e-tattoo, and the Bluetooth transmission of the data were unaffected by the WPT system. The depleted battery case was used to determine the time it would take to recharge a typical LiPo battery used in the chest e-tattoo while also confirming if the WPT system could provide enough power to operate the e-tattoo during the recharging of the device battery. Figure 5d shows a battery-free chest e-tattoo designed to be Qi-compatible with an Rx coil identical to the Tx coil in the hand band. The chest e-tattoo was completely powered by the WPT hand band to measure 3-axis seismocardiography (SCG) and one-channel electrocardiogram (ECG) from the chest[64] (Fig. 5e) and to transmit the data to a smartphone through Bluetooth Low Energy (Supplementary Video 3). Figure 5f demonstrates the wireless charging of a depleted LiPo battery (LP401230 105 mAh, PKCELL) connected to the chest e-tattoo while under e-tattoo operation, showing charging performance comparable to the commercial charger.

Electromagnetic radiation poses a potential hazard to human tissues, particularly within a wearable WPT system that operates at high frequency and high power. To evaluate the electromagnetic safety concerning the human tissue, we consider the SAR, defined as $SAR = \sigma \left|E_{\mathrm{rms}}\right|^2/\rho$, where σ and ρ denote the electrical conductivity and mass density of human tissue, respectively, and E_{rms} represents the root mean square of the electric field within the tissue. It is known that higher operating frequencies tend to yield higher SAR values due to increased tissue conductivity as frequency rises. Specifically, the power transmitted by a WPT operating at a low Industrial, Scientific, and Medical (ISM) frequency (13.56 MHz) and a high ISM frequency (40.68 MHz) must not exceed 2 and 0.3 W, respectively, due to a safety requirement of SAR ≤ 1.6 W/kg imposed by the FCC guidelines[49]. However, this limit presents a challenge for wearable WPT systems transmitting over 5 W as exemplified in our use case of smartphone charging.

It is less of a concern at Qi charging frequencies. A 3D electromagnetic FEA model was constructed to simulate the electromagnetic radiation at 130 kHz into the human tissue for handheld smartphone charging (see Fig. 5g(i), h(i) and "Methods" section)[75]. The maximum local SAR values on the palm turned out to be only 2.14 mW/kg (no magnetic shielding), 1.66 mW/kg (with Ferrofabric), and 0.93 mW/kg (with ferrite). All these values remain far below the safety limit of 1.6 W/kg (Fig. 5g(ii)). Similarly, a 3D FEA model consisting of the hand, our wearable charger, and the chest was built to simulate the e-tattoo charging (Fig. 5h(ii)), which reported maximum local SAR on the chest to be 1.68 mW/kg (no magnetic backplane), 2.25 mW/kg (Ferrofabric), and 3.33 mW/kg (ferrite), all of which are still far below the safety limit. The SAR was lowered by the magnetic backplane in the smartphone charging case but was elevated in e-tattoo charging mainly due to the magnetic layer on the palm concentrating the electric fields toward the chest free of a magnetic layer.

Body-loading effects could also negatively impact the WPT efficiency because the human body is a conductive medium, inducing eddy currents and power loss. However, given the low electrical conductivity of the tissues at the kHz frequency range, the body-loading effect on charging efficiency was found to be negligible by our simulation. Our results indicate that the maximum charging efficiency, with and without human tissue, remains comparable to each other (Supplementary Fig. 19).

Our device demonstrates higher received power and stretchability compared to state-of-the-art on-body WPT systems (Fig. 5i and Supplementary Fig. 20). This kind of watt-level on-body WPT is unachievable through NFC or RF as their SAR are much higher. In addition, alternative wearable transmitters with higher resistance, such as serpentine or wrinkle designs for metal films, or materials choices of EGaIn or MXene, would jeopardize either the charging efficiency or the thermal safety. Figure 5j shows our device is a significant step toward a practical wearable WPT in terms of efficiency and stretchability. A silver nanofiber-based antenna performs well in terms of efficiency (35%) and stretchability (100%) but their system is at a much higher frequency of 10 MHz, which leads to a better quality factor but much lower transmitted power (100 μW) than ours given the SAR limit[32]. We obtained this outstanding charging performance while ensuring mechanical robustness, thermal safety, and electromagnetic safety (Table 1). Furthermore, we observed no coil-to-coil efficiency degradation for 1000 cycles of 20% stretching on the

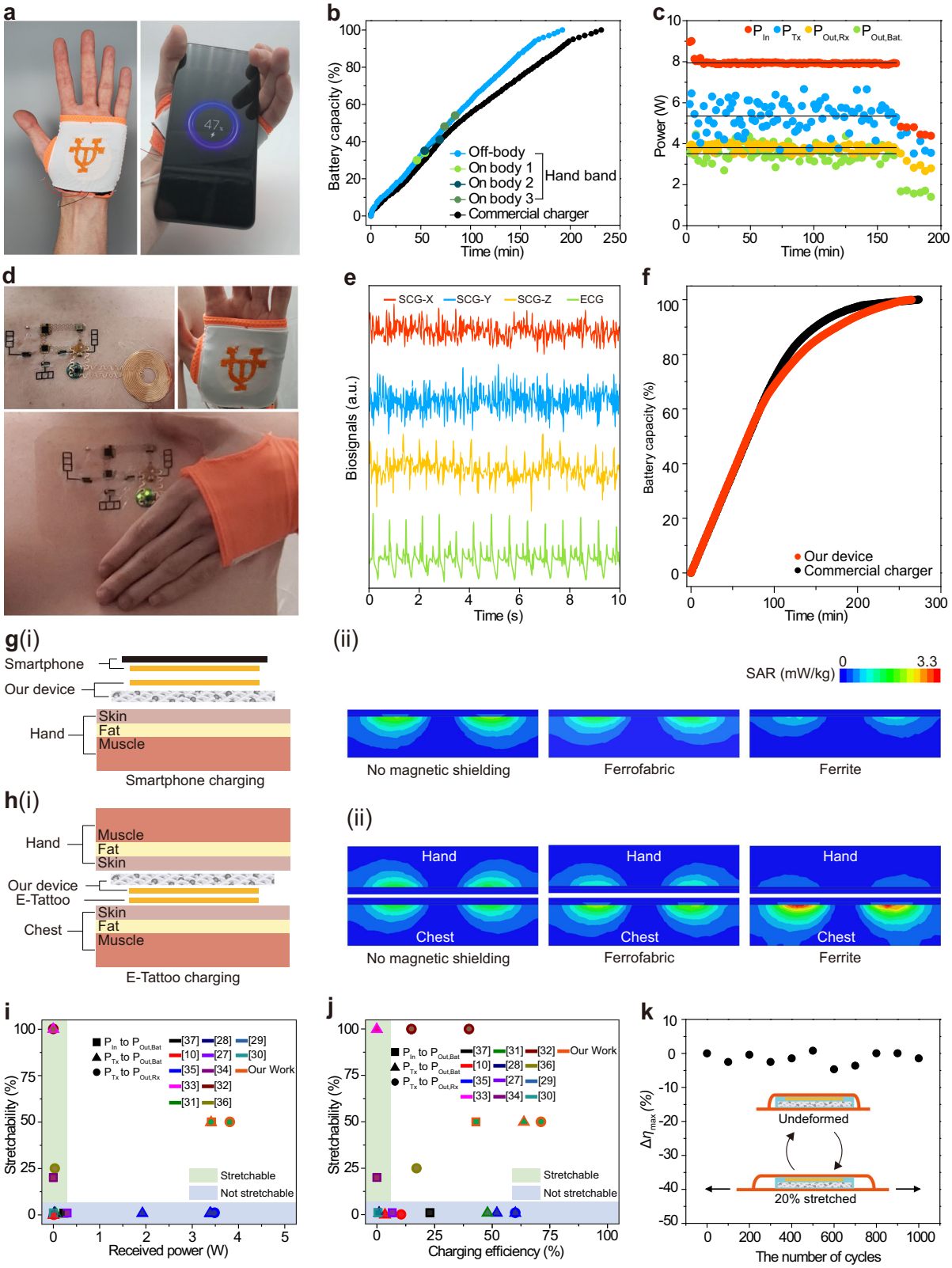

Fig. 5 | Proof-of-concept demonstration of smartphone and e-tattoo charging using the hand band. a Photographs of wireless charging of a smartphone. **b** Smartphone battery capacity over time, measured with our hand band placed on a table and worn on the palm compared with a commercial desktop wireless charger. **c** Measured four different power values as labeled in Fig. 3b in the smartphone charging. The horizontal lines on the graph indicate the average power in the normal charging range (0–95%). **d** Photographs of charging a chest e-tattoo using our device worn on the hand. **e** Seismocardiogram (SCG) and electrocardiogram (ECG) data collected through Bluetooth without any battery on the e-tattoo. **f** Battery capacity vs. time during the chest e-tattoo charging with a depleted LiPo battery using our hand band and the commercial wireless charger. **g**, **h** Simulated specific absorption rate (SAR) of the human hand during smartphone and e-tattoo charging. (i) A cross-sectional view of the electromagnetic model. (ii) Contour plots of the SAR with and without magnetic backplanes. Comparisons of state-of-the-art wearable WPT systems in terms of (**i**) stretchability vs. received power and **j** stretchability vs. charging efficiency. **k** Charging efficiency remained unchanged after cyclic stretches on the hand band.

hand band (Fig. 5k). Finally, it is noteworthy that our charger is easily applicable to wearable microgrid charging for various mobile and wearable devices located across the body, eliminating a separate mobile battery for each device.

We have devised an unobstructive and safe-to-wear WPT hand band capable of efficient charging of both handheld smartphones and wearable e-tattoo sensors via the Qi protocol. We have created a stretchable magnetic backplane, the Ferrofabric, with a unique combination of exceptional magnetic permeability and mechanical compliance. Through a holistic electromagnetic-structural-thermal analysis, we have achieved a fundamental understanding of the effects of coil material, coil thickness, magnetic backplane, and charging distance or misalignment on WPT performance in the kHz frequency range. We have elucidated a variety of loss mechanisms and found that the skin effect led to a critical thickness of the flexible Cu antenna. Further considerations of the proximity effect and the core loss yielded an optimal antenna-magnetic backplane design. We have also evaluated the user safety risks associated with joule heating and electromagnetic radiation. Our wearable WPT system showcases an unparalleled combination of wearability and power delivery to mobile and wearable devices, suggesting a new means of utilizing on-body or portable power sources without the hazards of charging cables. It also marks an exciting step toward the development of wearable microgrids wirelessly powering distributed mobile and wearable devices all over the body.

Methods

Fabrication of a hand band for wireless charging

The cut-and-paste fabrication method is used on a Cu foil (110-Annealed Cu, Nimrod) with a thickness of 25, 35, 50, and 75 μm is bonded to a single-sided thermal release tape (TRT, Semiconductor Equipment Corp.). Using a laser cutter (ProtoLaser U4, LPKF), we patterned the Cu foil to a 16-turn spiral coil shape. The excess Cu foil is removed from the TRT leaving the patterned coil area.

Next, we placed a (70 mm × 70 mm × 0.5 mm) pristine 38% bamboo 55% rayon, and 7% spandex fabric (Bamboo Rayon 4 Way Stretch with Spandex, APC Fabric Store) on one side with Tegaderm adhesives. To fabricate Ferrofabric, 4.5 mL of Ferrofluid (EMG 900, Ferrotec) is dripped onto the fabric using a pipette. Then, another Tegaderm is laminated onto the Ferrofabric for encapsulation. The excess peripheral Tegaderm near the Ferrofabric is cut to the extent that ferrofluid is not leaked.

Using a computerized sewing and embroidery machine (SE400, Brother), we created a palm hand band with a thumb hole. The hand band is a (140 mm × 90 mm × 0.5 mm) 20% spandex/80% nylon (Matte Milliskin 4 Way Stretch Nylon Spandex, Fabric Wholesale Direct). The two shorter sides (90 mm) consist of the top and bottom of the band and are made with a zigzag stitch pattern with a 100% spun polyester thread (Surelock Overlock Thread, Coats & Clark). The 140 mm open ends of the band are stitched in a zigzag pattern with 100% spun polyester thread to form a 50 mm thumb hole and join the two open ends of the band. Next, we performed a straight stitch pattern with a 100% spun polyester thread (Surelock Overlock Thread, Coats & Clark) to stitch the left, right, and top sides of a (75 mm × 75 mm × 0.5 mm) 20% spandex/80% nylon (Nylon Spandex Tricot Fabric 4 Way Stretch, FabricLA) onto the (140 mm × 90 mm × 0.5 mm) 20% spandex/80% nylon hand band to fabricate the pocket.

To integrate these into a fabric band for wireless charging, the Cu coil on TRT is transferred to a Tegaderm after heating at 125 °C for 30 s. The Tegaderm/Cu coil is transferred to the Tegaderm-encapsulated Ferrofabric to protect the other side of the Cu coil. Finally, the encapsulated coil and Ferrofabric are inserted into the pocket without using adhesives to allow strain isolation.

Fabric absorption test

The selected eight fabrics were tested; 100% cotton duck canvas (#2136323, Joann), 100% cotton muslin, (#7793672, Joann), 100% organic cotton sateen (Organic Cotton Sateen 500 Thread Count, Organic Cotton Plus), 100% cotton T-shirt (Essential Mens T-shirt pack, Hanes), 100% cotton fabric roll (300 Thread Count Cotton Fabric, Pellon), 100% cotton sheet (AmazonBasics Ultra-Soft Cotton Flat Sheet, Amazon), 38% bamboo 55% rayon and 7% spandex fabric (Bamboo Rayon 4 Way Stretch with Spandex, APC Fabric Store), 95% cotton and 5% spandex (Cotton Jersey Lyrca Spandex Knit Stretch, Fabric Wholesale Direct) to see which fabric composition was the best for ferrofluid absorption. Each fabric was cut into a (70 mm × 70 mm) square and then weighed. Next, 6 mL of an oil-based Ferrofluid (EFH1, Ferrotec) is dripped onto the fabric using a pipette and allowed to sit in the pool of excess Ferrofluid for 1 h. Then the fabric is lifted out of the pool of Ferrofluid and allowed to drip dry until no liquid drips from the fabric for at least 30 s. Next, the fabric is encapsulated on both sides with Tegaderm and then weighed.

Now that the weight before soaking and the weight after soaking with the 2 Tegaderms subtracted is recorded. The formula for mass absorption $\left(\frac{(\text{weight after soaking} - \text{weight before soaking})}{\text{weight before soaking}} \times 100\right)$ is used to determine the fabric absorption level.

Mechanical characterization

A Dynamic Mechanical Analyzer (RSA-G2, TA Instruments) was used to control displacement and to measure the applied force. (5 mm × 1 mm) samples including fabrics, Ferrofabric, encapsulated fabrics, and Tegaderm were stretched with a strain of 2.5%, and Young's modulus was calculated from the stress and strain curves.

Magnetic characterization

Three different samples including a fabric, Ferrofabric, and ferrofluid were tested to investigate the effect of the magnetic characteristics of each material. A Vibrating Sample Magnetometer (PPMS DynaCool, Quantum Design) was used to measure magnetization in a fabric used for fabricating Ferrofabric by applying magnetic fields ranging from −1 T to 1 T at room temperature. For the ferrofluid and Ferrofabric samples, M–H curves were obtained by a SQUID (MPMS3, Quantum Design) to perform high-resolution measurements. The magnetic field was swept from −1 T to 1 T at room temperature. The DC magnetic permeability was obtained from the initial slope of the M–H curve. To determine the AC magnetic permeability, the impedance simulated using commercial software (Maxwell, Ansys) was fit to the impedance of a coil on the Ferrofabric, which was measured using a vector network analyzer (E4080B, Keysight) at a frequency of 130 kHz. For WPT simulations, the AC relative permeability of 7.37 and a magnetic loss tangent of 0.091 were specified.

Electrical characterization

To evaluate the stability of the magnetic properties of Ferrofabric and obtain the real-time electrical properties of the coils, we performed the impedance measurement on the coil terminals at 130 kHz using an inductance, capacitance, and resistance (LCR) meter (E4980AL, Keysight).

To characterize the skin effect of a conductor, AC resistance and current density were simulated at 130 kHz using commercial software (COMSOL Multiphysics, COMSOL), and DC resistance was calculated from electrical conductivity and geometry. A conductor with a width of 1 mm for various thicknesses was used.

The impedance of a two-port network with inductive coupling was measured using two vector network analyzers (E4080B, Keysight and ZNH8, Rohde & Schwarz). The measured scattering parameters were converted into inductance and resistance for charging efficiency calculations.

The inductance and resistance values were also obtained using commercial FEA software (Maxwell, Ansys). This was achieved by simulating WPT for the device operating at a frequency of 130 kHz. In the simulation model, we included a transmitter coil and a receiver coil with a vertical gap of 1 mm for smartphone charging and 0.5 mm for e-tattoo charging (Supplementary Fig. 6). Each magnetic layer was located in close proximity to its respective coil to provide magnetic shielding. The entire device was

surrounded by air to simulate electromagnetic fields within a 3D domain. For the excitation, both the Tx and Rx coils were driven by sinusoidal currents at a frequency of 130 kHz. To evaluate electromagnetic safety in Fig. 5g, h, human tissue layers including skin ($\sigma = 0.00057$ S/m), fat ($\sigma = 0.0434$ S/m), muscle ($\sigma = 0.367$ S/m)[75] were included in the model. In addition, we considered further enhanced magnetic shielding by introducing a flexible ferrite sheet with an AC relative permeability of 159.8 and a magnetic loss tangent of 0.039.

Thermal characterization

To assess the long-term thermal safety of the human tissue during extended device operation, the steady-state temperature distribution of the human hand and the device was simulated using commercial software (COMSOL Multiphysics, COMSOL). Detailed geometry and material property information can be found in Fig. 4f and Supplementary Fig. 15. The simulation model encompassed a smartphone with an Rx coil, a hand band, a Tx coil, Ferrofabric, encapsulation, and human tissue layers. In the simulation, we took into account the joule heating generated by currents passing through the Tx and Rx coils as detailed in Supplementary Note 1. The heat generation from the normal operation of the smartphone was set to 1 W. To consider the thermal behavior of human tissue, metabolism and blood perfusion were modeled. On all outer surfaces, free convection was applied with the ambient room temperature of 21 °C and a convective heat transfer coefficient of 10 $W/(m^2 \cdot K)$.

A digital thermometer (TMD-56, Amprobe) was used to measure the palm temperature and fabric band temperature. Each thermometer probe was located at a point with the in-plane maximum temperature determined by thermal simulation.

Durability test

A hydraulic stretcher (MTS) was used to stretch a hand band containing an encapsulated Tx coil and Ferrofabric with a tensile strain of 20% at a cyclic loading frequency of 1 Hz for 1000 cycles. Resistance and inductance were measured using an LCR meter (E4980AL, Keysight) throughout the testing process. In addition, charging efficiency was assessed after every 100 cycles to evaluate the device's performance over 1000 cycles.

Wireless charging of a smartphone

The charging test consisted of a mobile phone (Mi Mix 3, Xiaomi), a 22 W wireless power charging board (WCT-15W1CFFPD Evaluation Board, NXP), and a commercial charger (Mi Wireless Charger MDY-09-EU, Xiaomi). The hand band system is worn on the hand and three different battery levels on the mobile phone are charged for 10 min to make sure it correlates with the on-table charging.

The FOD was adjusted through a graphic user interface using Freemaster 3.1 and the IC chip was flashed with the new calibration values through the Multilink Universal FX JTAG programmer and CodeWarrior 11.1 software.

The on-table power measurements were performed with a load tester (A3 Q7-T USB Tester, Atorch) for the DC input power, two hall current sensors (ACS772LCB050BPFFT, Allegro) and an oscilloscope (MDO3014, Tektronix) for the AC transmitted and received voltage and current values, and two phone apps (Battery Charge Meter Pro, AndroidCodeX and AccuBattery, Digibites) and a timer for the DC output power. The load tester was placed between the power source and the board. The current sensors were placed in series with the board and coil. The oscilloscope probes for the voltage were attached across the coil ends. The experiment consisted of charging a phone with complete depletion of the battery to full battery capacity. The device was placed on the wireless charger and powered on. After the device was powered up a measurement was taken on the load tester, oscilloscope, and the two phone apps for every battery capacity percentage increase. The method of capture was performed in this order; timer was recorded, then the oscilloscope measurement was saved, followed by unlocking the phone and opening the first phone app and recording the data, then opening the second phone app and recording the data, finally the phone was locked, and the process repeated for each battery capacity percent increase. Consent was obtained for publication of the photographs and videos.

Wireless charging of a chest e-tattoo

The charging of the chest e-tattoo was performed with the ECG/SCG chest e-tattoo from a 5 W Board (NXQ1TXH5 Evaluation Board, NXP), and a mobile power source (PLM09ZM 10,000 mAh)[64]. The chest e-tattoo was placed on the chest without a power source. Then the hand band charging system was worn on the hand and powered by a mobile power bank. Next, the Cu coil on the chest was aligned with the Cu coil on the palm and used to power the chest e-tattoo to demonstrate clean data collection and data transfer. The 5 W board power transfer was measured with a debugger (NXQ1TXH5DB135, NXP).

The in-house fabricated Cu coil has a different value of inductance of 15.18 μH than the traditional coil 6.3 μH. Therefore, the series capacitance in the circuit needs to be changed from 364 to 100 nF in order to operate in the desired frequency range of 130 kHz.

The 5 W board FOD requires a simple change of a few resistors R8 to accommodate for the equivalent AC loss resistance ($R8 = 390,000 * (\text{AC loss} - 0.135)/(1.470 - \text{AC loss})$) in the system and R14 is altered ($R14 = 0.00983/C$) to accurately calculate the power loss internally in the IC chip. Then the FOD threshold needs to be changed through R9 in order to maintain a stable connection for WPT ($R9 = 390,000 * \text{threshold}/(3.3 - \text{threshold})$).

The next experiment took a chest e-tattoo placed on a table powered by a discharged battery (LP401230 105 mAh) and was charged with the Cu coil with the Ferrofabric and commercial charger. Then the charging coil is aligned with the chest e-tattoo coil and the battery level is measured with a multimeter (UT58D, UNI-T), and the elapsed time was recorded until fully charged. Consent was obtained for publication of the photographs and videos.

Hand clenching of the palm charger

The cyclic clenching of the palm charger was performed by wearing the hand band system with the 5 W board and clenching the hand into a fist. The band was closed for 500 clinches and the ability to charge the phone was tested every 100 clenches by placing the mobile phone on the palm charger. Consent was obtained for publication of the video.

Data availability

Additional data related to this paper may be requested from the corresponding authors upon reasonable request.

Received: 22 April 2024; Accepted: 27 October 2024;
Published online: 08 November 2024

References

1. Pu, X., Hu, W. & Wang, Z. L. Toward wearable self-charging power systems: the integration of energy-harvesting and storage devices. *Small* **14**, 1702817 (2018).
2. Ray, T. R. et al. Bio-integrated wearable systems: a comprehensive review. *Chem. Rev.* **119**, 5461–5533 (2019).
3. Luo, Y. et al. Technology roadmap for flexible sensors. *ACS Nano* **17**, 5211–5295 (2023).
4. Li, H. et al. E-tattoos: toward functional but imperceptible interfacing with human skin. *Chem. Rev.* **124**, 3220–3283 (2024).
5. Yin, L., Kim, K. N., Trifonov, A., Podhajny, T. & Wang, J. Designing wearable microgrids: towards autonomous sustainable on-body energy management. *Energy Environ. Sci.* **15**, 82–101 (2022).
6. Yin, J. et al. Smart textiles for self-powered biomonitoring. *Med-X* **1**, 3 (2023).
7. Yin, L. et al. A self-sustainable wearable multi-modular E-textile bioenergy microgrid system. *Nat. Commun.* **12**, 1542 (2021).

8. Niu, S. et al. A wireless body area sensor network based on stretchable passive tags. *Nat. Electron.* **2**, 361–368 (2019).
9. Niu, S., Wang, X., Yi, F., Zhou, Y. S. & Wang, Z. L. A universal self-charging system driven by random biomechanical energy for sustainable operation of mobile electronics. *Nat. Commun.* **6**, 8975 (2015).
10. Tian, X. et al. Wireless body sensor networks based on metamaterial textiles. *Nat. Electron.* **2**, 243–251 (2019).
11. Hajiaghajani, A. et al. Textile-integrated metamaterials for near-field multibody area networks. *Nat. Electron.* **4**, 808–817 (2021).
12. Chaari, M. Z., Al-Rahimi, R. & Aghzout, O. High power wireless power transfer for the future of the battle field challenges. *Secur. Def. Q.* **4**, 9–26 (2022).
13. Magnuson, S. Power-hungry devices challenge Army researchers. *Natl. Def.* **101**, 37–38 (2017).
14. Mardonova, M. & Choi, Y. Review of wearable device technology and its applications to the mining industry. *Energies* **11**, 547 (2018).
15. Hofer, I. & Cannesson, M. Is wireless the future of monitoring? *Anesth. Analg.* **122**, 305–306 (2016).
16. Wahlman, A., Clavin, C. T., Keller, R. A., Georgi, D. M. & Ayers, J. R. *Assessment of the Challenges Associated with Individual Battlefield Power: Addressing the Power Budget Burdens of the Warfighter and Squad* (Institute for Defense Analyses, 2022).
17. Masrur, M. A. & Cox, M. A unique military application of wireless power transfer: wireless charging through a vehicle seat with simplified design considerations. *IEEE Ind. Electron. Mag.* **13**, 19–30 (2019).
18. Yao, W., Ng, K. F., Xiao, H., Wang, K. & Mao, Y. In *2022 IEEE 9th International Conference on Power Electronics Systems and Applications (PESA)* (IEEE, 2022).
19. Kim, C. Y. et al. Soft subdermal implant capable of wireless battery charging and programmable controls for applications in optogenetics. *Nat. Commun.* **12**, 535 (2021).
20. Yu, X. et al. Skin-integrated wireless haptic interfaces for virtual and augmented reality. *Nature* **575**, 473–479 (2019).
21. Li, J., Dong, Y., Park, J. H. & Yoo, J. Body-coupled power transmission and energy harvesting. *Nat. Electron.* **4**, 530–538 (2021).
22. Kim, D.-H. et al. Epidermal electronics. *Science* **333**, 838–843 (2011).
23. Joo, H. et al. Soft implantable drug delivery device integrated wirelessly with wearable devices to treat fatal seizures. *Sci. Adv.* **7**, eabd4639 (2021).
24. Li, C. et al. Flexible perovskite solar cell-driven photo-rechargeable lithium-ion capacitor for self-powered wearable strain sensors. *Nano Energy* **60**, 247–256 (2019).
25. Liu, M., Qian, F., Mi, J. & Zuo, L. Biomechanical energy harvesting for wearable and mobile devices: state-of-the-art and future directions. *Appl. Energy* **321**, 119379 (2022).
26. Amjadi, M., Yoon, Y. J. & Park, I. Ultra-stretchable and skin-mountable strain sensors using carbon nanotubes–Ecoflex nanocomposites. *Nanotechnology* **26**, 375501 (2015).
27. Seo, Y.-S. et al. Wireless power transfer for a miniature gastrostimulator. In *2012 42nd European Microwave Conference* (IEEE, 2012).
28. Alrashdan, F. T. et al. Wearable wireless power systems for 'ME-BIT' magnetoelectric-powered bio implants. *J. Neural Eng.* **18**, 045011 (2021).
29. Kod, M. et al. An approach to improve the misalignment and wireless power transfer into biomedical implants using meandered wearable loop antenna. *Wirel. Power Transf.* **2021**, 1–12 (2021).
30. Yu, Z. et al. MagNI: a magnetoelectrically powered and controlled wireless neurostimulating implant. *IEEE Trans. Biomed. Circuits Syst.* **14**, 1241–1252 (2020).
31. Lin, R. et al. Digitally-embroidered liquid metal electronic textiles for wearable wireless systems. *Nat. Commun.* **13**, 2190 (2022).
32. Zhang, Y. et al. High precision epidermal radio frequency antenna via nanofiber network for wireless stretchable multifunction electronics. *Nat. Commun.* **11**, 1–10 (2020).
33. Barron, E. J. III, Peterson, R. S., Lazarus, N. & Bartlett, M. D. Mechanically cloaked multiphase magnetic elastomer soft composites for wearable wireless power transfer. *ACS Appl. Mater. Interfaces* **12**, 50909–50917 (2020).
34. Jeong, H. et al. Modular and reconfigurable wireless e-tattoos for personalized sensing. *Adv. Mater. Technol.* **4**, 1900117 (2019).
35. Teng, L., Zhu, L., Handschuh-Wang, S. & Zhou, X. Robust, multiscale liquid-metal patterning enabled by a sacrificial sealing layer for flexible and wearable wireless powering. *J. Mater. Chem. C* **7**, 15243–15251 (2019).
36. Xu, S. et al. Stretchable batteries with self-similar serpentine interconnects and integrated wireless recharging systems. *Nat. Commun.* **4**, 1543 (2013).
37. Dautta, M. et al. Wireless Qi-powered, multinodal and multisensory body area network for mobile health. *IEEE Internet Things J.* **8**, 7600–7609 (2021).
38. Liu, Y. et al. Epidermal mechano-acoustic sensing electronics for cardiovascular diagnostics and human-machine interfaces. *Sci. Adv.* **2**, e1601185 (2016).
39. Sun, Y., Choi, W. M., Jiang, H., Huang, Y. Y. & Rogers, J. A. Controlled buckling of semiconductor nanoribbons for stretchable electronics. *Nat. Nanotechnol.* **1**, 201–207 (2006).
40. Yang, S. et al. "Cut-and-paste" manufacture of multiparametric epidermal sensor systems. *Adv. Mater.* **27**, 6423–6430 (2015).
41. Ye, J., Xing, Z.-R., Gao, J.-Y. & Liu, J. Liquid metal coil. *Mater. Today Commun.* **32**, 104120 (2022).
42. Lin, R. et al. Wireless battery-free body sensor networks using near-field-enabled clothing. *Nat. Commun.* **11**, 444 (2020).
43. Sun, D. et al. Investigating flexible textile-based coils for wireless charging wearable electronics. *J. Ind. Text.* **50**, 333–345 (2020).
44. Barreto, J., Kaddour, A.-S., An, H. S., Sheperd, R. & Georgakopoulos, S. V. Optimal embroidered wearable WPT systems with liquid metal nanoparticles. In *2021 IEEE International Symposium on Antennas and Propagation and USNC-URSI Radio Science Meeting (APS/URSI)* (IEEE, 2021).
45. Rahman, M. S., Huddy, J. E., Hamlin, A. B. & Scheideler, W. J. Broadband mechanoresponsive liquid metal sensors. *npj Flex. Electron* **6**, 71 (2022).
46. Lazarus, N. & Bedair, S. Improved power transfer to wearable systems through stretchable magnetic composites. *Appl. Phys. A* **122**, 1–7 (2016).
47. Lu, X., Wang, P., Niyato, D., Kim, D. I. & Han, Z. Wireless charging technologies: fundamentals, standards, and network applications. *IEEE Commun. Surv. Tutor.* **18**, 1413–1452 (2016).
48. Meile, L., Ulrich, A. & Magno, M. Wireless power transmission powering miniaturized low power IoT devices: a revie. In *2019 IEEE 8th International Workshop on Advances in Sensors and Interfaces (IWASI)* (IEEE, 2019).
49. Mohanarangam, K., Palagani, Y. & Choi, J. Evaluation of specific absorption rate in three-layered tissue model at 13.56 MHz and 40.68 MHz for inductively powered biomedical implants. *Appl. Sci.* **9**, 1125 (2019).
50. Samsung Electronics. SAR Information. https://www.samsung.com/sar/sarMain?site_cd=&prd_mdl_name=SM-S928U&selNatCd=US&languageCode=EN (2024)
51. Tian, X. et al. Implant-to-implant wireless networking with metamaterial textiles. *Nat. Commun.* **14**, 4335 (2023).
52. Siman-Tov, E., Tseng, V. F.-G., Bedair, S. S. & Lazarus, N. Increasing the range of wireless power transmission to stretchable electronics. *IEEE Trans. Microw. Theory Tech.* **66**, 5021–5030 (2018).
53. Gao, W., Wang, L., Wang, X. & Liu, H. Magnetic driving flowerlike soft platform: Biomimetic fabrication and external regulation. *ACS Appl. Mater. Interfaces* **8**, 14182–14189 (2016).

54. Lazarus, N., Meyer, C. D., Bedair, S. S., Slipher, G. A. & Kierzewski, I. M. Magnetic elastomers for stretchable inductors. *ACS Appl. Mater. Interfaces* **7**, 10080–10084 (2015).
55. Hu, X., Fu, Y., Wu, T. & Qu, S. Study of non-uniform axial magnetic field induced deformation of a soft cylindrical magneto-active actuator. *Soft Matter* **17**, 7498–7505 (2021).
56. Diguet, G., Froemel, J., Muroyama, M. & Ohtaka, K. Tactile sensing using magnetic foam. *Polymers* **14**, 834 (2022).
57. Li, J. et al. Design and fabrication of microfluidic mixer from carbonyl iron–PDMS composite membrane. *Microfluid. Nanofluidics* **10**, 919–925 (2011).
58. Denver, H., Heiman, T., Martin, E., Gupta, A. & Borca-Tasciuc, D.-A. Fabrication of polydimethylsiloxane composites with nickel nanoparticle and nanowire fillers and study of their mechanical and magnetic properties. *J. Appl. Phys.* **106**, 064909 (2009).
59. Pirmoradi, F. N., Cheng, L. & Chiao, M. A magnetic poly (dimethylesiloxane) composite membrane incorporated with uniformly dispersed, coated iron oxide nanoparticles. *J. Micromech. Microeng.* **20**, 015032 (2009).
60. Lazarus, N., Bedair, S. S. & Smith, G. L. Creating 3D printed magnetic devices with ferrofluids and liquid metals. *Addit. Manuf.* **26**, 15–21 (2019).
61. Lazarus, N. & Meyer, C. Stretchable inductor with liquid magnetic core. *Mater. Res. Express* **3**, 036103 (2016).
62. Liu, J., Yu, M.-Y., Yu, Z.-Z. & Nicolosi, V. Design and advanced manufacturing of electromagnetic interference shielding materials. *Mater. Today* **66**, 245–272 (2023).
63. Maaß, M., Griessner, A., Steixner, V. & Zierhofer, C. Reduction of eddy current losses in inductive transmission systems with ferrite sheets. *BioMed. Eng. OnLine* **16**, 1–18 (2017).
64. Bhattacharya, S. et al. A chest-conformable, wireless electro-mechanical e-tattoo for measuring multiple cardiac time intervals. *Adv. Electron. Mater.* **9**, 2201284 (2023).
65. Huang, W. et al. Monolithic mtesla-level magnetic induction by self-rolled-up membrane technology. *Sci. Adv.* **6**, eaay4508 (2020).
66. Bury, E., Thiagarajan, S., Lazarus, N. & Koh, A. Ferrofluid high internal phase emulsion polymer foams for soft, magnetic materials. *J. Magn. Magn. Mater.* **563**, 169921 (2022).
67. Shen, Q. et al. Liquid metal-based soft, hermetic, and wireless-communicable seals for stretchable systems. *Science* **379**, 488–493 (2023).
68. Lee, E. S. & Choi, B. G. Calculation methodologies of complex permeability for various magnetic materials. *Electronics* **10**, 2167 (2021).
69. Taalla, R. V., Arefin, M. S., Kaynak, A. & Kouzani, A. Z. A review on miniaturized ultrasonic wireless power transfer to implantable medical devices. *IEEE Access* **7**, 2092–2106 (2019).
70. Jow, U.-M. & Ghovanloo, M. Modeling and optimization of printed spiral coils in air, saline, and muscle tissue environments. *IEEE Trans. Biomed. Circuits Syst.* **3**, 339–347 (2009).
71. Mohammad, M., Choi, S. & Elbuluk, M. E. Loss minimization design of ferrite core in a DD-coil-based high-power wireless charging system for electrical vehicle application. *IEEE Trans. Transp. Electrific.* **5**, 957–967 (2019).
72. Wang, H. et al. Folding and bending planar coils for highly precise soft angle sensing. *Adv. Mater. Technol.* **5**, 2000659 (2020).
73. Stier, A. et al. Stretchable tattoo-like heater with on-site temperature feedback control. *Micromachines* **9**, 170 (2018).
74. Ryu, H. et al. Materials and device designs for wireless monitoring of temperature and thermal transport properties of wound beds during healing. *Adv. Healthc. Mater.* **13**, 2302797 (2024).
75. Rhee, J. et al. Wireless torque and power transfer using multiple coils with LCC-S topology for implantable medical drug pump. *Sensors* **21**, 8150 (2021).

Acknowledgements

Nanshu Lu acknowledges the support from the U.S. Army Research Laboratory (ARL) under Corporative Agreement W911NF-19-2-0036 and the U.S. Army Research Office (ARO) under Cooperative Agreement W911NF-19-2-0333. The views and conclusions contained in this review are those of the authors and should not be interpreted as representing the official policies, either expressed or implied, of the ARL, the ARO, or the U.S. government. S.K. acknowledges the support from Philip C. and Linda L. Lewis Foundation Graduate Fellowship. J.W. acknowledges the support from the multiyear Virginia & Ernest Cockrell, Jr. Fellowship in Engineering.

Author contributions

S.K. and J.W. contributed equally to the work under the guidance of Nathan Lazarus and Nanshu Lu. Nanshu Lu, Nathan Lazarus, S.K., and J.W. conceived and designed the research. S. K. and J. W. designed the experiments and carried out the characterization. S.K. and P.K. performed simulations and analysis. J.W. prepared the materials. S.B., H.N., J.H., I.T., H.H., A.F., P.P., J.Z., and E.P. performed the experiments. S.K., J.W., E.P., Nanthan Lazarus, and Nanshu Lu wrote the manuscript. All the authors discussed the results and commented on the manuscript.

Competing interests

The authors declare no competing interests.

Additional information

Supplementary information The online version contains supplementary material available at https://doi.org/10.1038/s41528-024-00363-7.

Correspondence and requests for materials should be addressed to Nathan Lazarus or Nanshu Lu.